NANO LETTERS

Letter

pubs.acs.org/NanoLett

Rational Design of Plasmonic Nanoparticles for Enhanced Cavitation and Cell Perforation

Rémi Lachaine,[†] Christos Boutopoulos,[†,‡] Pierre-Yves Lajoie,[†] Étienne Boulais,[†,§] and Michel Meunier*[,†]

[†]Laser Processing and Plasmonics Laboratory, Engineering Physics Department, École Polytechnique de Montréal, Montréal, Québec H3C 3A7, Canada

[‡]School of Physics and Astronomy, SUPA, University of St. Andrews, North Haugh, St. Andrews, KY16 9SS, United Kingdom

[§]Department of Chemistry, Université de Montréal, Montréal, Québec H3C 3J7, Canada

Supporting Information

ABSTRACT: Metallic nanoparticles are routinely used as nanoscale antenna capable of absorbing and converting photon energy with subwavelength resolution. Many applications, notably in nanomedicine and nanobiotechnology, benefit from the enhanced optical properties of these materials, which can be exploited to image, damage, or destroy targeted cells and subcellular structures with unprecedented precision. Modern inorganic chemistry enables the synthesis of a large library of nanoparticles with an increasing variety of shapes, composition, and optical characteristic. However, identifying and tailoring nanoparticles morphology to specific applications remains challenging and limits the development of efficient nanoplasmonic technologies. In this work, we report a strategy for the rational design of gold plasmonic nanoshells (AuNS) for the efficient ultrafast laser-based nanoscale bubble generation and cell membrane perforation, which constitute one of the most crucial challenges toward the development of effective gene therapy treatments. We design an in silico rational design framework that we use to tune AuNS morphology to simultaneously optimize for the reduction of the cavitation threshold while preserving the particle structural integrity. Our optimization procedure yields optimal AuNS that are slightly detuned compared to their plasmonic resonance conditions with an optical breakdown threshold 30% lower than randomly selected AuNS and 13% lower compared to similarly optimized gold nanoparticles (AuNP). This design strategy is validated using time-resolved bubble spectroscopy, shadowgraphy imaging and electron microscopy that confirm the particle structural integrity and a reduction of 51% of the cavitation threshold relative to optimal AuNP. Rationally designed AuNS are finally used to perforate cancer cells with an efficiency of 61%, using 33% less energy compared to AuNP, which demonstrate that our rational design framework is readily transferable to a cell environment. The methodology developed here thus provides a general strategy for the systematic design of nanoparticles for nanomedical applications and should be broadly applicable to bioimaging and cell nanosurgery.

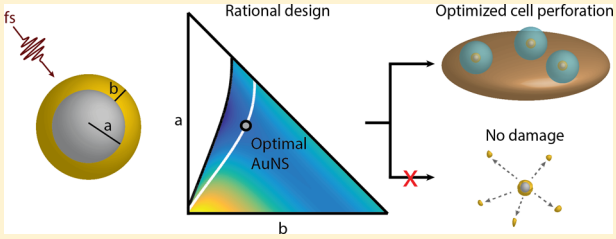

KEYWORDS: *Plasmon, nanobubble, ultrafast laser, nanoshell, cell nanosurgery, optoporation*

Metal nanostructures hold a great potential for guiding and manipulating light at subwavelength scales due to localized surface plasmon resonance (LSPR).[1−4] Over the last decades, their unique ability to locally enhance electromagnetic fields has enabled using light to interact with cellular and molecular structures with unprecedented precision.[5−7] In particular, this capability has been leveraged to develop new diagnostic and therapeutic approaches in the context of targeted gene[8−11] and drug[12,13] delivery, tissue imaging,[14−17] and photothermal therapy.[18,19]

The development of plasmon-based nanomedicine has been greatly supported by the intense effort made by chemists and material scientists to synthesize nanoscale particles with diverse shape and composition, providing tunable plasmon resonance wavelength and near-field patterns.[20−23] Notably, structures with near-infrared resonance such as gold nanoshells (AuNS)[24] and gold nanorods[25] have been developed to match the transparency window of biological tissues, ensuring minimal collateral damage and maximal penetration depth for biomedical applications.[26] Moreover, AuNS have been used for enhanced biosensing,[27] cancer treatment,[28] gene silencing,[29] DNA release,[30] and steam generation.[31,32]

Recently, nonlinear interaction of photons with plasmonic particles has brought new opportunities for enhancing optical processes in the near-field, including Raman scattering and frequency mixing,[33] surface nanoablation[34] and nanocavitation.[35,36] Typically, nanoparticles specifically designed for these nonlinear processes are challenging to optimize because their efficiency not only depends on the resonance cross sections but more importantly on the near-field enhancement nanolocalization. Often, the magnitude of the near-field enhancement must

Received: February 8, 2016
Revised: March 29, 2016
Published: April 5, 2016

DOI: 10.1021/acs.nanolett.6b00562
Nano Lett. 2016, 16, 3187−3194

be balanced with resistive losses that may heat and irreversibly damage the particle,[37,38] deteriorating their plasmonic properties. In such conditions, simply tuning the plasmonic resonance to the incident laser wavelength is not optimal and a more involved rational design strategy must be employed. The complexity inherent to nonlinear processes thus justifies the development of a systematic method that could enable the rational design of nanomaterials with optical properties tailored to specific applications, which we here address.

In this work, we sought to enhance the near-field mediated cavitation process that uses nonlinear photoionization and photoexcitation of a quasi-free electron plasma in the near-field of water-immersed nanoparticles to generate nanoscale bubbles.[9,36,39] When targeted to a cell, these particles transiently perforate the membrane and can lead to efficient cell transfection in the context of gene therapy.[40] Here, we aim to rationally design AuNS with the objective of minimizing the laser energy that is required to induce cavitation while avoiding irreversible damage to the nanostructure (Figure 1). We arbitrarily

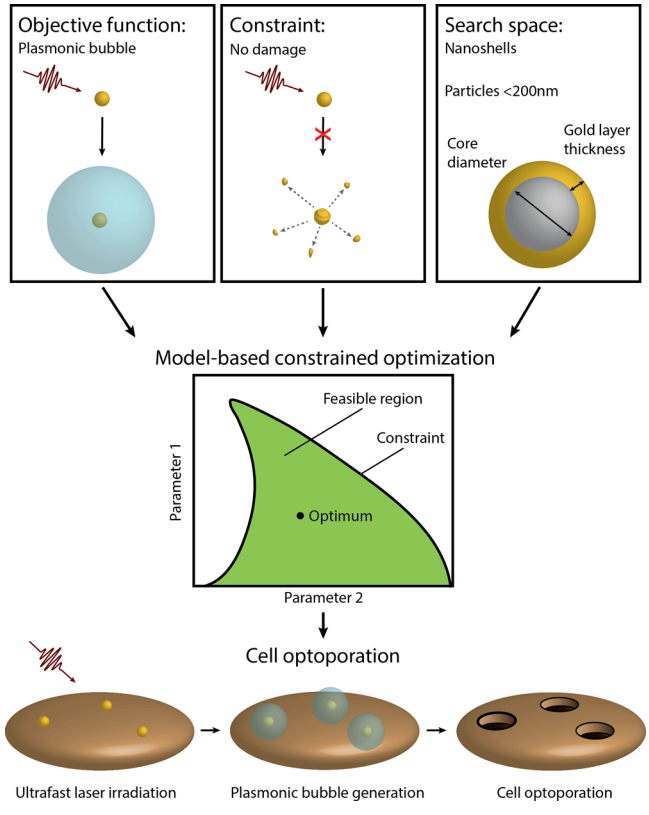

Figure 1. Principle of the in silico rational design of plasmonic nanostructures for plasmon-enhanced nanocavitation and cell optoporation. We aim to minimize the fluence required to generate plasmonic bubbles (objective function) while avoiding damage to nanoparticle (constraint). The example given here is for AuNS with a total diameter under 200 nm. Our model-based constrained optimization framework yields the parameters describing the AuNS morphology that optimizes the objective function while respecting the constraints over the parameter search space. These designed particles enable bubble generation and cell membrane perforation at lower fluence.

restrained the design space to silica−gold nanoshells with a total diameter under 200 nm, irradiated with near-infrared (800 nm) ultrashort (70 fs) pulses. We present a computational method that enables designing in silico AuNS that can yield robust near-field cavitation while limiting resistive losses below a theoretically predicted damage level. We provide numerical evidence that these designed AuNS should lead to significant improvement compared to suboptimal AuNS and rationally designed gold spherical nanoparticles (AuNP). Using time-resolved spectroscopy, shadowgraphy imaging, and structural characterization, we then demonstrate that synthesized AuNS behave accordingly to the theoretical predictions and that our rational design methodology enables reducing the cavitation threshold by 51% compared to 150 nm AuNP, while preserving their structural integrity. Finally, these optimal AuNS are shown to efficiently optoperforate breast cancer cells with a fluence 33% lower than 150 nm AuNP, showing the transferability of our rational design framework to a biological context.

First, we developed a rational design framework that leverage the unique tunability of water-immersed AuNS, which optical properties can be adjusted across the visible and near-infrared range by a careful modification of their silica core radius and gold layer thickness.[41] Mie theory[42,43] was used to calculate the AuNS optical properties. Briefly, we utilized the morphology-dependent near-field enhancement magnitude (Figure 2a) and absorption cross sections (Figure 2b) calculated from the Mie theory to evaluate the fluence-morphology loci corresponding to nanocavitation and irreversible damage to the particle and used this result to optimize the AuNS geometrical characteristics.

In the ultrafast regime, laser-induced cavitation is associated with the creation of a nanoscale plasma in the enhanced near-field.[36] In a first approximation, it is commonly assumed that optical breakdown and bubble generation occurs when a critical plasma density $\rho = 10^{21}$ cm^{-3} is reached[44] although lower density ($\rho = 10^{18}$−10^{20} cm^{-3}) have also been reported to induce breakdown.[45] Similar to previous work,[36,44] we used a combination of Keldysh photoionization theory in strong electric field[46] and avalanche ionization[44] to estimate the laser intensity required to reach optical breakdown ($\rho = 10^{21}$ cm^{-3}) for each AuNS morphology, thus defining a fluence-morphology cavitation locus (Supporting Note 1).

Similarly, irreversible damage to the particle is due to energy absorption within the AuNS due to resistive losses. From the absorption cross-section and considering gold thermodynamic properties and the fast energy deposition time that enables neglecting energy diffusion, we calculated the maximum temperature reached by AuNS (Supporting Note 2). We associated the irreversible damage threshold to AuNS reaching the fusion temperature of gold (1337 K),[47] although significant damage can realistically occur at much lower temperature.[48] This defines a fluence-morphology locus associated with irreversible damage to the AuNS.

Combining the fluence-morphology damage and cavitation loci defines a four-dimensional diagram that informs to which "state" the laser-particle system behavior corresponds: (N) noncavitating intact AuNS, (D) damaged noncavitating AuNS, (B) cavitating (bubble) intact AuNS, and (B+D) cavitating (bubble) damaged AuNS (Figure 2c). At a fluence of 0 J/cm^2, all AuNS are in state (N). As the fluence is increased, the state of each AuNS evolves along a trajectory that depends on their morphology. Our optimization procedure consists in identifying what morphology defines a state-trajectory that penetrates state (B) directly from state (N), thus avoiding state (D) and (B+D), and to minimize the fluence at which this state transition occurs (Figure 2d).

We further require that the laser fluence at the cavitation threshold is at least twice the laser fluence at the damage threshold.

DOI: 10.1021/acs.nanolett.6b00562
Nano Lett. 2016, 16, 3187−3194

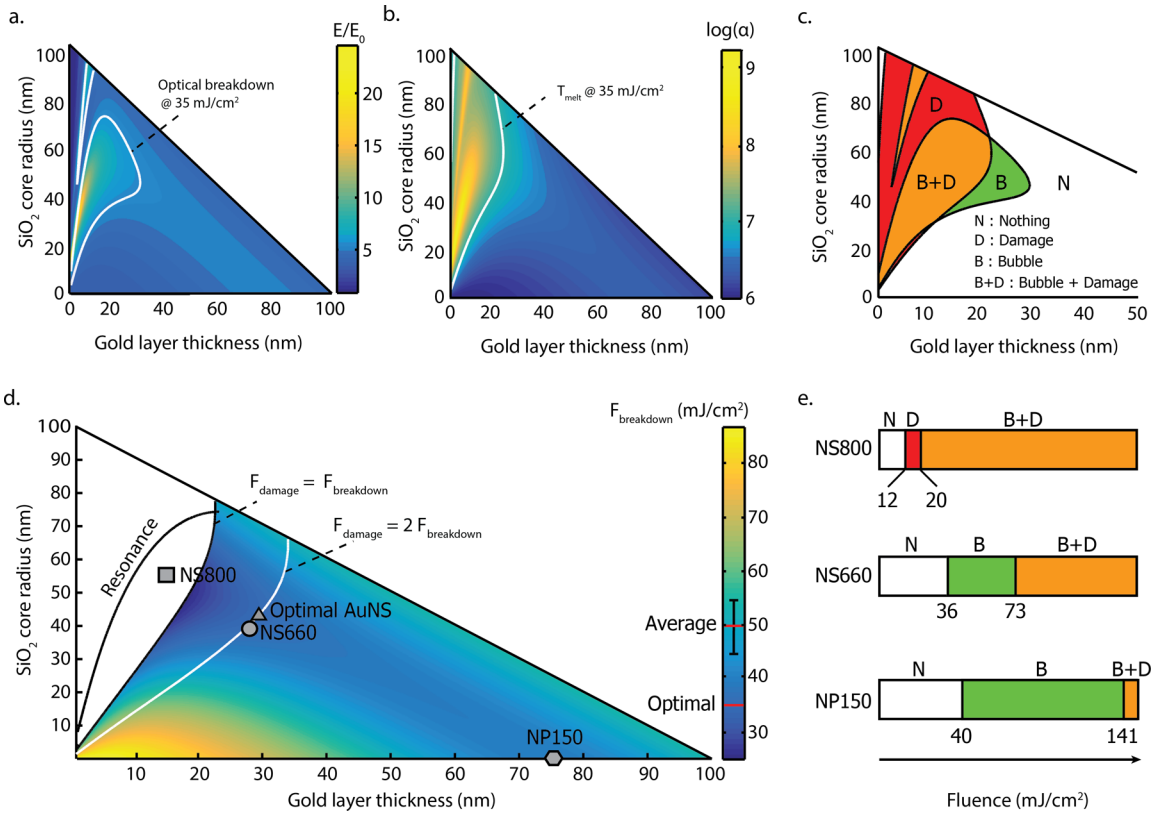

Figure 2. In silico rational design strategy of AuNS. The two optimizing parameters are SiO_2 core radius and gold layer thickness. (a) Maximal near-field enhancement as a function of AuNS dimensions. The white lines define the locus of cavitation ($\rho = 10^{21}$ cm^{-3}) for a fluence of 35 mJ/cm^2, a judicious fluence example that corresponds to the breakdown threshold of NS660. (b) Linear absorption coefficient as a function of AuNS dimensions. The white line indicates the locus of irreversible damage for a fluence of 35 mJ/cm^2. (c) The four different "states" defined by the intersection of the cavitation and irreversible damage loci: (N) noncavitating intact AuNS, (D) damaged noncavitating AuNS, (B) cavitating (bubble) intact AuNS, and (B+D) cavitating (bubble) damaged AuNS. (d) Threshold fluences for nanocavitation as a function of AuNS dimensions. The plasmon resonance condition at 800 nm is indicated by the solid black line. The factor of safety ($F_{damage} = 2F_{breakdown}$) is indicated by the solid white line. The optimal AuNS (triangle) and the selected AuNS (NS800 (square), NS660 (circle), and NP150 (hexagon)) are shown. (e) The state trajectories of NS800, NS660, and NP150 as a function of fluence.

This arbitrary "factor of safety" ensures a reasonable margin between the cavitation and the damage threshold that leaves some flexibility for experimental variability and the adequate tuning of nanobubble sizes. Randomly selected AuNS that correspond to this stricter criterion present a cavitation threshold of 50 ± 5 mJ/cm^2 on average (Supporting Note 3). In comparison, optimal AuNS (42 nm core radius, 29 nm shell thickness) reduce this threshold by 3 standard deviations, down to 35 mJ/cm^2, which justify our approach. Importantly, optimal AuNS are quite far from the plasmon resonance condition, which demonstrate that a delicate balance between energy absorption and near-field enhancement must be reached to ensure optimality. Interestingly, for the special case of AuNP (core-radius of 0 nm), the optimal morphology (diameter = 150 nm) yields a cavitation threshold 13% higher than optimal AuNS, which suggests that the extra tunability of AuNS is beneficial to near-field mediated cavitation processes. The diameter of optimal AuNP is in agreement with previous reports.[49]

We next sought to validate experimentally our in silico rational design strategy. We thoroughly investigated and characterized the nanocavitation process and structural damage sustained by three particles of carefully selected morphologies. These morphologies were chosen to examine the behavior of particles that yield very different trajectories in the state diagram (Figure 2e). The first one (label: NS800, bare AuNS with 56 nm core radius and 15 nm shell thickness, from nanoComposix, Inc.) follows the trajectory (N) → (D) → (B+D) without reaching state (D). This particle is resonant at 800 nm and is predicted not to induce cavitation without sustaining irreversible damage. The second one (label: NS660, bare AuNS with 39 nm core radius, 28 nm shell thickness, from nanoComposix, Inc.) follows the trajectory (N) → (B) → (B+D) and is close (3% higher cavitation threshold) to optimal AuNS (42 nm core radius, 29 nm shell thickness). The third one (label: NP150, bare AuNP with 150 nm diameter, from Nanopartz) follows a similar trajectory and corresponds to the optimal AuNP.

First, we used the scattering[36,39,50] and shadowgraphy[51] techniques to assess the nanobubble generation threshold for each of the nanoparticles (Supporting Note 4). Those techniques were used because nanobubbles cannot be studied by conventional high speed cameras due to their extremely short lifetime (<150 ns). Briefly, an ultrafast pump laser beam (Ti:sapphire, 800 nm, 70 fs, 10 Hz, Spitfire, Spectra-Physics) was coaligned with two probe laser beams. The first probe laser (He:Ne 633 nm, 2 mW, continuous-wave, Thorlabs) measured the scattering signal coming from the bubbles. The second probe laser (Nd:YAG, 532 nm, 6 ns, 10 Hz, Brilliant b, Quantel) excited a fluorescent dye (rhodamine) to yield a broad light emission pulse that was used to take shadowgraphic images of the bubbles (Figure S1a). Note that the local fluence irradiating

DOI: 10.1021/acs.nanolett.6b00562
Nano Lett. 2016, 16, 3187−3194

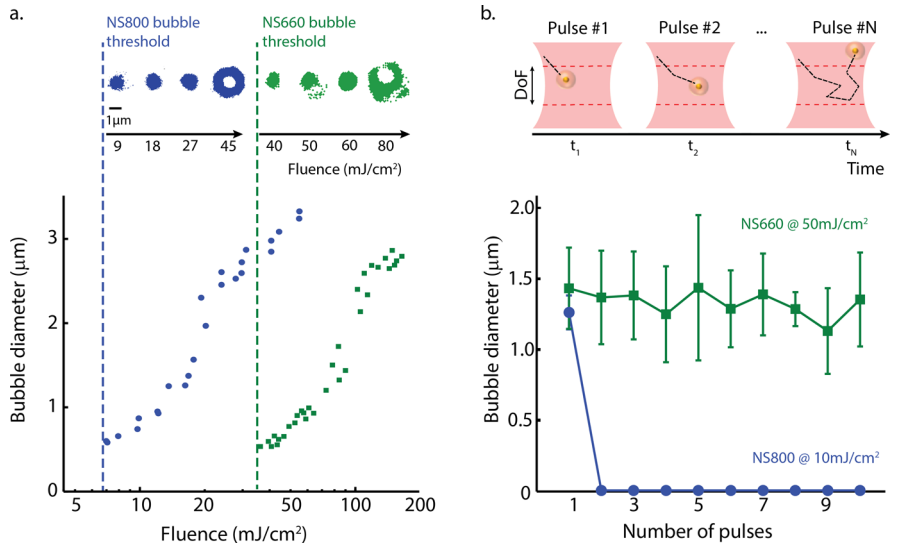

Figure 3. Experimental characterization of AuNS-assisted nanocavitation. (a) Experimental bubble threshold for the NS800 and the NS660 using both shadowgraphy and scattering methods. (b) Consecutive bubbles generated from a single particle. Thirteen single-NS660 were irradiated with 50 mJ/cm^2 pulses and tracked. Consecutive bubbles were measured using the shadowgraphy technique and their diameters measured (green line). The same methodology was applied to single-NS800 at 10 mJ/cm^2 but no consecutive bubbles have been observed (blue line).

each AuNS was considered rather than the average fluence within the whole pump Gaussian beam (Supporting Note 5).

Plasmonic nanobubbles were detected for fluences of 7−9 and 35−40 mJ/cm^2 for the NS800 and NS660, respectively (Figure 3a). In comparison, plasmonic nanobubbles were detected at much higher fluences for 150 nm AuNP (∼77 mJ/cm^2) (Figure S2). These results follow the general trend predicted by the simulation and confirm that the rationally designed AuNS (NS660) provide a significant reduction of the cavitation threshold relative to 150 nm AuNP.

While the measured cavitation threshold for NS660 (∼35 mJ/cm^2) is in excellent agreement with simulation (36 mJ/cm^2), the one for NS800 (∼7 mJ/cm^2) is significantly lower than what was predicted at the design stage (∼20 mJ/cm^2). This discrepancy is probably due to the contribution of the energy absorbed in the AuNS to the cavitation process, which can become non-negligible for resonant particles.[52] More complex modeling would be required to include these effects at the rational design stage but is beyond the scope of this work because these particles would inevitably be characterized by a high absorption cross-section, a low damage threshold, and would consequently be suboptimal. This hypothesis is consistent with observations showing that multiple consecutive bubbles could be generated from NS660, while only a single one could be generated with NS800 (Figure 3b). In this experiment, single particles irradiated with multiple, consecutive laser pulses at 10 Hz were tracked while bubble generation was monitored using shadowgraphy imaging. We conclude from these experiments that NS660 could generate multiple bubbles while NS800 could not. This suggests that energy absorption in NS800 leads to an irreversible degradation of their plasmonic properties, which is in agreement with modeling predictions.

Second, we thoroughly investigated the structural integrity of AuNS following laser irradiation using transmission electron microscopy (TEM). Quartz cuvettes containing 1 mL of particles solution were irradiated at 1 kHz for 1 h at three different fluences around the ones where plasmonic nanobubbles could be detected (Figure 4a,d). The solution was magnetically stirred during irradiation to ensure uniform and complete irradiation of the particles. Analysis of TEM imaging (Figure S3) reveals the presence of three distinct populations of particles (intact, cracked, and melted particles) with proportions that vary according to the irradiation fluence (Figure 4b,e). Importantly, at a fluence where bubbles could be detected (40 mJ/cm^2), the proportion of cracked and melted particles remains relatively low (∼19%) for the NS660 sample. This confirms that NS660 can generate nanobubbles while preserving structural integrity, which is in agreement with simulation predictions. On the other hand, NS800 sustains heavy damage (∼98% of cracked and melted particles) when irradiated with a fluence corresponding to the bubble detection threshold (8 mJ/cm^2), which is also consistent with our modeling.

In order to establish the damage threshold with more precision, we monitored the shift of the plasmon peak that result from laser irradiation. Plasmon resonance being extremely sensitive to the structure and dielectric properties of the nanoparticle, thorough monitoring of the plasmon resonance should inform on the structural damage sustained by the particle following irradiation. Similarly to the TEM study, quartz cuvettes containing 1 mL of particles solution were irradiated at 1 kHz for 1 h at a given fluence (Figure S1b). A visible-near IR spectrometer (Ocean Optics USB4000 VIS-NIR) was used to monitor the plasmon resonance in real-time (Figure 4c,f). The damage threshold was defined as the inflection point of the peak position as a function of fluence.

Damage thresholds of 65 and 6 mJ/cm^2 were measured for NS660 and NS800, respectively. The measured damage threshold for NS660 is in relatively good agreement with the simulation result (73 mJ/cm^2), while the simulated threshold for NS800 is slightly higher (12 mJ/cm^2). This discrepancy could be explained by nonlinear absorption and nonthermal damage that has been reported to occur for resonant particles.[3] Nevertheless, these measurements confirm that NS660 trajectory in the state diagram goes directly from state (N) to state (B) and thus that cavitation occurs for fluences lower than the damage threshold. In opposition, NS800 are damaged at fluences lower than the fluences that are required to generate bubbles, as predicted by the rational design methodology. This important

DOI: 10.1021/acs.nanolett.6b00562
Nano Lett. 2016, 16, 3187−3194

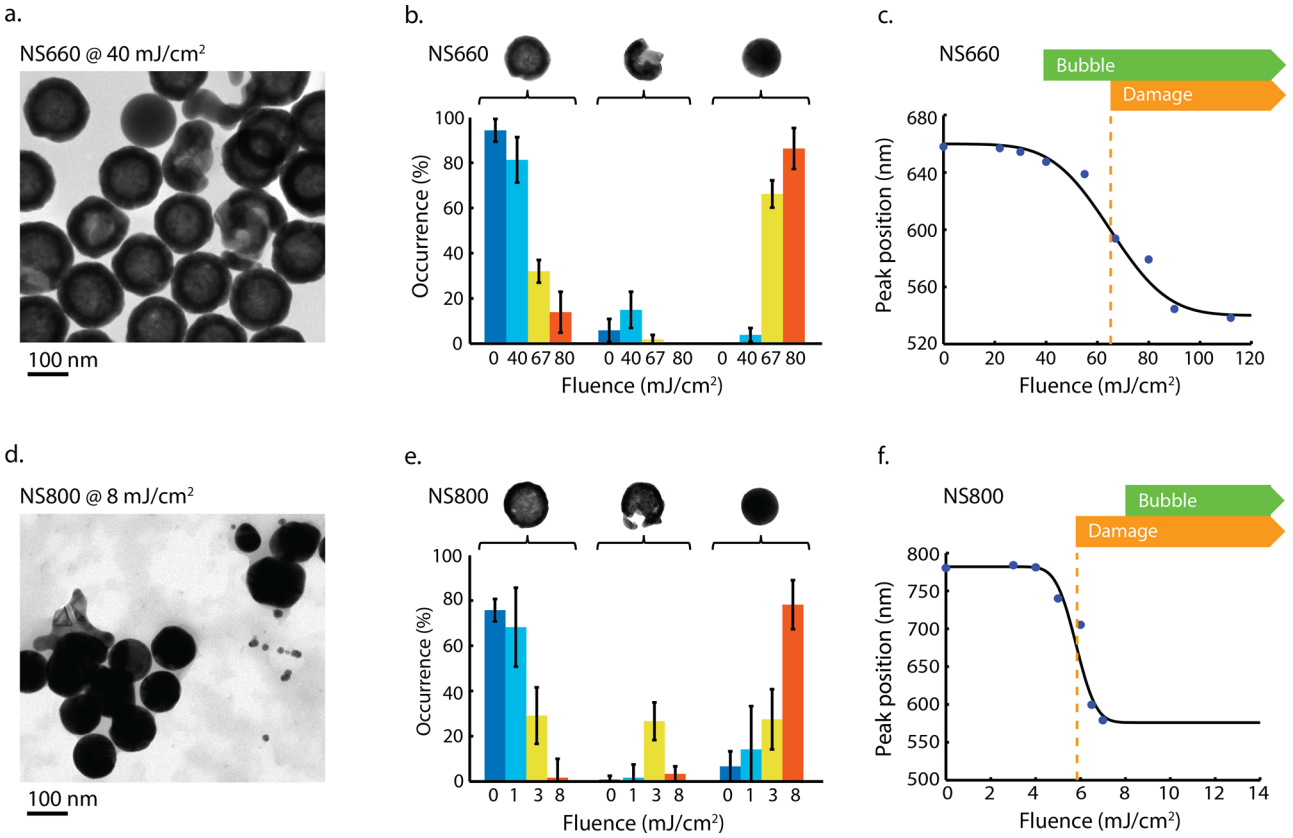

Figure 4. Characterization of the structural damage sustained by AuNS following laser irradiation. (a) TEM image of the NS660 after 40 mJ/cm^2 irradiation. (b) Proportion of intact, cracked, and melted NS660. Dark blue bars correspond to 0 mJ/cm^2, light blue to 40 mJ/cm^2, yellow to 67 mJ/cm^2, and orange to 80 mJ/cm^2. (c) Plasmonic resonance peak position of the NS660 after laser irradiation as a function of fluence. Damage and bubble threshold are indicated. (d) TEM image of the NS800 after 8 mJ/cm^2 irradiation. (e) Proportion of intact, cracked, and melted NS800. Dark blue bars correspond to 0 mJ/cm^2, light blue to 1 mJ/cm^2, yellow to 3 mJ/cm^2, and orange to 8 mJ/cm^2. (f) Plasmonic resonance peak position of the NS800 after laser irradiation as a function of fluence. Damage and bubble threshold are indicated.

result confirms that tuning the plasmonic resonance peak to the laser wavelength does not lead to an optimized design in this case and highlights the importance of our in silico rational design procedure to rigorously optimize the plasmonic nanoparticles for nonlinear processes.

Finally, we sought to evaluate the performance of our rationally designed AuNS for perforating the membrane of human breast cancer cells (MDA-MB-231). Cancer cells were routinely seeded onto glass bottom dishes (1×10^5 cells, 19.63 cm^2, MatTek) and grown in Dulbecco's Modified Eagle's Medium (DMEM) supplemented with antibiotics and 10% fetal bovine serum (FBS, Invitrogen). Before laser treatment, the cells were incubated with 6×10^8 AuNS/mL in 3 mL cell culture medium for 2 h. These AuNS were provided by nanoComposix with lipoic acid conjugation to increase nonspecific binding to cell membranes. Afterward, the cells were washed twice with phosphate-buffered saline and finally phenol red free medium was added to the dishes. The presence of AuNS on the cell membrane was confirmed using dark-field microscopy[53] (Figure S2b). The cells were then irradiated with 70 fs, 800 nm laser pulses at 200 Hz. Areas of 1.25 mm × 10 mm have been scanned with a 400 μm Gaussian laser spot ($1/e^2$) at a speed of 10 mm/s, giving ~64 pulses per particle. The cell perforation rate was measured from the uptake of cell impermeant green fluorescent dye (calcein, high purity, final concentration 2.5 μM) introduced 5 min before laser irradiation. Cell death was measured by adding a red fluorescent dye (propidium iodide (PI), final concentration 1.5 μM) to the cells 1 h after irradiation. PI is cell impermeant and stained only those cells having nonhealed cell membranes 1 h post laser treatment. The cell viability was defined as the ratio of viable (nonred) cells on the total number of cells. The cell perforation rate was defined as the ratio of viable green cells on the total number of cells. Note that in the special case of both green and red cells, those were counted as dead. The proportion of viable and dead cells was counted manually from 61 fluorescence images similar to Figure 5a,c for a total of 7750 cells. The optoporation threshold was defined as the first fluence yielding more than 10% perforation rate. Control experiments were performed using dishes without AuNS and laser fluence of 180 mJ/cm^2 (~10 times the AuNS assisted optoporation threshold). No green dye uptake was observed (Figure S4). Three independent experiments were performed in separate dishes.

We measured an optoporation threshold of 40 mJ/cm^2 when using the rationally designed NS660 (Figure 5b). Importantly, this threshold is in good agreement with the bubble detection threshold for NS660 (40 mJ/cm^2 vs 35 mJ/cm^2), similar to previous reports with AuNP.[54] A maximal perforation rate of 61% with viability over 90% was obtained at a slightly higher fluence of 60 mJ/cm^2. This fluence however remains lower than the damage threshold (65 mJ/cm^2), implying that the laser process leaves the particle intact. Compared to AuNPs, the fluence required for optoporation is significantly lower (Figure S5). Note that perforation rates of more than 80% have

DOI: 10.1021/acs.nanolett.6b00562
Nano Lett. 2016, 16, 3187−3194

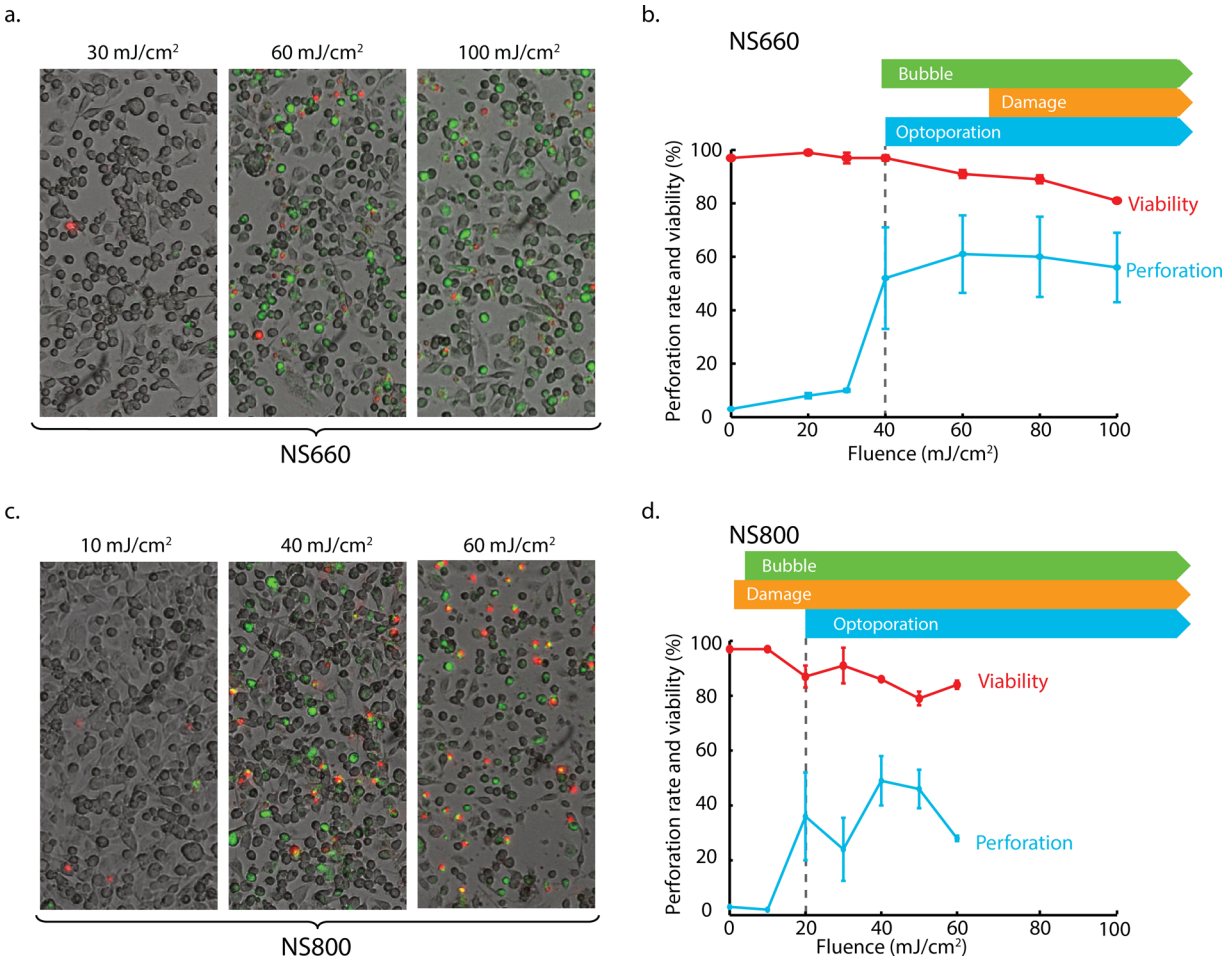

Figure 5. Breast cancer cell perforation with AuNS. Green and red staining indicate membrane perforation and cell death, respectively. (a) Fluorescence image of the cells at 30, 60, and 100 mJ/cm^2 using NS660. (b) Perforation rate and viability as a function of fluence using NS660. The perforation threshold is 40 mJ/cm^2 and the maximal perforation rate is 61 ± 15% at 60 mJ/cm^2. Bubble, damage, and optoporation thresholds are indicated. (c) Fluorescence image of the cells at 10, 40, and 60 mJ/cm^2 using NS800. (d) Perforation rate and viability as a function of fluence using NS800. The perforation threshold is 20 mJ/cm^2 and the maximal perforation rate is 49% at 40 mJ/cm^2. Bubble, damage, and optoporation thresholds are indicated.

been reported using 100 nm AuNP[54] but were achieved with 100 mJ/cm^2, almost twice as large as what we achieved in this report. This confirms that our in silico rational design framework successfully identified AuNS that could efficiently perforate cell membranes at low fluence while preserving their structural integrity.

In comparison, suboptimal resonant NS800 could achieve optoporation at even lower fluence (20−40 mJ/cm^2) (Figure 5d). Unlike NS660, the optoporation fluence for NS800 is much higher than the fluence required to generate bubbles (7 mJ/cm^2). This behavior is probably due to the heavy damage sustained by the resonant AuNS, which prevents the generation of multiple bubbles that are hypothesized to help enhancing the perforation rate. In addition, the presence of small gold fragments from damaged particles raises significant concerns relative to long-term toxicity.[55]

In summary, we have successfully developed and demonstrated the use of an in silico rational design framework to tailor particle morphology to a specific nonlinear plasmon-enhanced process. Specifically, we designed AuNS that minimize the fluence required to induce cavitation in a water medium while preserving their structural integrity. These simulation predictions were thoroughly verified using time-resolved spectroscopy and electron microscopy, and the tested AuNS were shown to behave according to the simulated predictions (Figure 6). Also, the cavitation enhancement and robustness of the designed AuNS were shown to be transferrable to a biological context, and breast cancer cells were perforated using the optimized robust particles with unprecedentedly low fluences while preserving AuNS structural integrity.

In the process of analyzing our computational optimization framework, we uncovered an interesting structure-performance relationship that brings important insight into the design of plasmonic particles for specific applications. Importantly, optimal AuNS were shown to deviate significantly from the plasmon resonance condition. Consequently, one has to be especially careful when applying the usual paradigm that consists in adjusting the plasmon resonance to the irradiation wavelength to optimize a nonlinear plasmonic process. In addition, visualizing plasmon-enhanced process as trajectories in a morphology-fluence space was helpful to provide intuition on defining relevant design criteria.

We believe that a similar in silico rational design process could be applied for the optimization of a large number of plasmon-based technologies, including photothermal therapy,[18,19] cell nanosurgery,[6] surface-enhanced Raman scattering,[33] dark-field

DOI: 10.1021/acs.nanolett.6b00562
Nano Lett. 2016, 16, 3187−3194

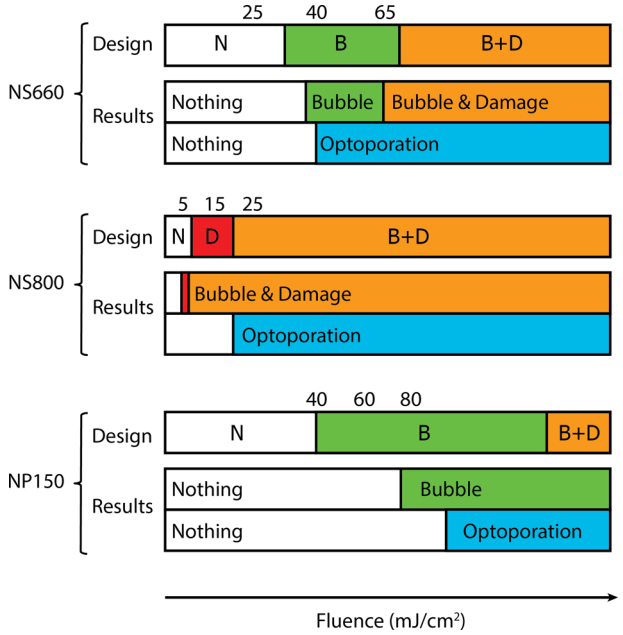

Figure 6. Comparison of the design and experimental state-trajectory for NS660, NS800, and NP150.

imaging,[19] and energy-harvesting.[2] Although it was here applied to plasmonic gold nanoshells, combined with efficient minimization algorithms,[56] this procedure could be generalized to enable the in silico screening of large libraries of plasmonic materials, structures, and irradiation conditions to identify potential candidates tailored to specific applications. This type of virtual screening approach, popular in the drug discovery process[57] and recently applied in the field of organic electronics[58] could help foster discovery in the field of nonlinear plasmonics.

■ ASSOCIATED CONTENT

Supporting Information

The Supporting Information is available free of charge on the ACS Publications website at DOI: 10.1021/acs.nanolett.6b00562.

Additional details on our modeling approach; precision on the definition of randomly selected particles; precisions on the irradiation and shadowgraphy imaging setups; precision on the definition of fluence; bubble and damage thresholds for 150 nm AuNPs; additional TEM imaging of irradiated AuNS; control optoporation of MDA-MB-231 cancer cells without nanoparticles; and optoporation efficiency for 150 nm AuNPs. (PDF)

■ AUTHOR INFORMATION

Corresponding Author

*E-mail: michel.meunier@polymtl.ca.

Author Contributions

R.L. designed the rational design strategy, performed scattering and shadowgraphy bubble detection, performed TEM imaging of all particles, irradiated the cells samples, and analyzed all data; C.B. performed shadowgraphy imaging and prepared the cell samples; P.-Y.L. performed TEM imaging of NS800; E.B designed the rational design strategy and analyzed data; M.M. supervised the work and analyzed data; R.L, E.B., and M.M wrote the manuscript. All authors have given approval to the final version of the manuscript.

Notes

The authors declare no competing financial interest.

■ ACKNOWLEDGMENTS

The authors would like to thank the Natural Science and Engineering Research Council (NSERC) and Le Fond Québecois de la Recherche sur la Nature et les Technologies (FQRNT) for financial support. C.B. acknowledges funding from the EU under a Marie Curie Fellowship, FP7-PEOPLE-2013- IOF, project reference 624888. Adrien Dagallier, Nicolas Le Hir, Ali Hatef, Alexandra Thibeault-Eybalin, David Rioux and Éric Bergeron are acknowledged for valuable discussions. Yves Drolet is acknowledged for technical support.

■ REFERENCES

(1) Berweger, S.; Atkin, J. M.; Xu, X. G.; Olmon, R. L.; Raschke, M. B. *Nano Lett.* **2011**, *11* (10), 4309−4313.
(2) Novotny, L.; van Hulst, N. *Nat. Photonics* **2011**, *5* (2), 83−90.
(3) Plech, A.; Kotaidis, V.; Lorenc, M.; Boneberg, J. *Nat. Phys.* **2006**, *2* (1), 44−47.
(4) Brongersma, M. L.; Halas, N. J.; Nordlander, P. *Nat. Nanotechnol.* **2015**, *10* (1), 25−34.
(5) Anker, J. N.; Hall, W. P.; Lyandres, O.; Shah, N. C.; Zhao, J.; Van Duyne, R. P. *Nat. Mater.* **2008**, *7* (6), 442−453.
(6) Csaki, A.; Garwe, F.; Steinbrück, A.; Maubach, G.; Festag, G.; Weise, A.; Riemann, I.; König, K.; Fritzsche, W. *Nano Lett.* **2007**, *7* (2), 247−253.
(7) Zijlstra, P.; Paulo, P. M. R.; Orrit, M. *Nat. Nanotechnol.* **2012**, *7* (6), 379−382.
(8) Baumgart, J.; Humbert, L.; Boulais, É.; Lachaine, R.; Lebrun, J. J.; Meunier, M. *Biomaterials* **2012**, *33* (7), 2345−2350.
(9) Boulais, E.; Lachaine, R.; Hatef, A.; Meunier, M. *J. Photochem. Photobiol., C* **2013**, *17*, 26−49.
(10) Baumgart, J.; Bintig, W.; Ngezahayo, A; Willenbrock, S.; Murua Escobar, H.; Ertmer, W.; Lubatschowski, H.; Heisterkamp, A. *Opt. Express* **2008**, *16* (5), 3021−3031.
(11) Lukianova-Hleb, E. Y.; Samaniego, A. P.; Wen, J.; Metelitsa, L. S.; Chang, C. C.; Lapotko, D. O. *J. Controlled Release* **2011**, *152* (2), 286−293.
(12) Yavuz, M. S.; Cheng, Y.; Chen, J.; Cobley, C. M.; Zhang, Q.; Rycenga, M.; Xie, J.; Kim, C.; Song, K. H.; Schwartz, A. G.; Wang, L. V.; Xia, Y. *Nat. Mater.* **2009**, *8* (12), 935−939.
(13) Rwei, A. Y.; Wang, W.; Kohane, D. S. *Nano Today* **2015**, *10* (4), 451−467.
(14) Bardhan, R.; Lal, S.; Joshi, A.; Halas, N. J. *Acc. Chem. Res.* **2011**, *44* (10), 936−946.
(15) Vendrell, M.; Maiti, K. K.; Dhaliwal, K.; Chang, Y.-T. *Trends Biotechnol.* **2013**, *31* (4), 249−257.
(16) Mallidi, S.; Larson, T.; Tam, J.; Joshi, P. P.; Karpiouk, A.; Sokolov, K.; Emelianov, S. *Nano Lett.* **2009**, *9* (8), 2825−2831.
(17) Lozano, N.; Al-Jamal, W. T.; Taruttis, A.; Beziere, N.; Burton, N. C.; Van den Bossche, J.; Mazza, M.; Herzog, E.; Ntziachristos, V.; Kostarelos, K. *J. Am. Chem. Soc.* **2012**, *134* (32), 13256−13258.
(18) Huang, X. H.; El-Sayed, I. H.; Qian, W.; El-Sayed, M. A. *J. Am. Chem. Soc.* **2006**, *128* (6), 2115−2120.
(19) Loo, C.; Lowery, A.; Halas, N. J.; West, J.; Drezek, R. *Nano Lett.* **2005**, *5* (4), 709−711.
(20) Schreiber, R.; Do, J.; Roller, E.-M.; Zhang, T.; Schüller, V. J.; Nickels, P. C.; Feldmann, J.; Liedl, T. *Nat. Nanotechnol.* **2013**, *9* (1), 74−78.
(21) Manjavacas, A; García de Abajo, F. J. *Nat. Commun.* **2014**, *5*, 3548.
(22) Sun, W.; Boulais, E.; Hakobyan, Y.; Wang, W. L.; Guan, A.; Bathe, M.; Yin, P. *Science* **2014**, *346* (6210), 1258361.
(23) Rioux, D.; Meunier, M. *J. Phys. Chem. C* **2015**, *119* (23), 13160−13168.
(24) Halas, N. *MRS Bull.* **2005**, *30* (05), 362−367.

DOI: 10.1021/acs.nanolett.6b00562
Nano Lett. 2016, 16, 3187−3194

(25) Huang, X.; Neretina, S.; El-Sayed, M. A. *Adv. Mater.* **2009**, *21* (48), 4880−4910.
(26) Weissleder, R. *Nat. Biotechnol.* **2001**, *19* (4), 316−317.
(27) Hirsch, L. R.; Jackson, J. B.; Lee, A.; Halas, N. J.; West, J. L. *Anal. Chem.* **2003**, *75* (10), 2377−2381.
(28) Gobin, A. M.; Lee, M. H.; Halas, N. J.; James, W. D.; Drezek, R. A.; West, J. L. *Nano Lett.* **2007**, *7* (7), 1929−1934.
(29) Huschka, R.; Barhoumi, A.; Liu, Q.; Roth, J. A.; Ji, L.; Halas, N. J. *ACS Nano* **2012**, *6* (9), 7681−7691.
(30) Huschka, R.; Zuloaga, J.; Knight, M. W.; Brown, L. V.; Nordlander, P.; Halas, N. J. *J. Am. Chem. Soc.* **2011**, *133* (31), 12247−12255.
(31) Neumann, O.; Neumann, A. D.; Silva, E.; Ayala-Orozco, C.; Tian, S.; Nordlander, P.; Halas, N. J. *Nano Lett.* **2015**, *15* (12), 7880−7885.
(32) Neumann, O.; Urban, A. S.; Day, J.; Lal, S.; Nordlander, P.; Halas, N. J. *ACS Nano* **2013**, *7* (1), 42−49.
(33) Kauranen, M.; Zayats, A. V. *Nat Phot.* **2012**, *6* (11), 737−748.
(34) Robitaille, A.; Boulais, E.; Meunier, M. *Opt. Express* **2013**, *21* (8), 9703−9710.
(35) Kotaidis, V.; Dahmen, C.; Von Plessen, G.; Springer, F.; Plech, A. *J. Chem. Phys.* **2006**, *124* (18), 184702.
(36) Boulais, É.; Lachaine, R.; Meunier, M. *Nano Lett.* **2012**, *12* (9), 4763−4769.
(37) Aguirre, C. M.; Moran, C. E.; Young, J. F.; Halas, N. J. *J. Phys. Chem. B* **2004**, *108* (22), 7040−7045.
(38) Akchurin, G.; Khlebtsov, B.; Akchurin, G.; Tuchin, V.; Zharov, V.; Khlebtsov, N. *Nanotechnology* **2008**, *19* (1), 015701.
(39) Lachaine, R.; Boulais, É.; Meunier, M. *ACS Photonics* **2014**, *1* (4), 331−336.
(40) Bergeron, E.; Boutopoulos, C.; Martel, R.; Torres, A.; Rodriguez, C.; Niskanen, J.; Lebrun, J.-J.; Winnik, F. M.; Sapieha, P.; Meunier, M. *Nanoscale* **2015**, *7*, 17836−17847.
(41) Oldenburg, S. J.; Averitt, R. D.; Westcott, S. L.; Halas, N. J. *Chem. Phys. Lett.* **1998**, *288* (2−4), 243−247.
(42) Mie, G. *Ann. Phys.* **1908**, *330* (3), 377−445.
(43) Le Ru, E. C.; Etchegoin, P. G. *Principles of Surface-Enhanced Raman Spectroscopy and Related Plasmonic Effects*; Elsevier: Amsterdam, 2009.
(44) Vogel, A.; Noack, J.; Hüttman, G.; Paltauf, G. *Appl. Phys. B: Lasers Opt.* **2005**, *81* (8), 1015−1047.
(45) Kennedy, P. K.; Hammer, D. X.; Rockwell, B. A. *Prog. Quantum Electron.* **1997**, *21* (3), 155−248.
(46) Keldysh, L. V. *J. Exp. Theor. Phys.* **1965**, *20* (5), 1307−1314.
(47) Ekici, O.; Harrison, R. K.; Durr, N. J.; Eversole, D. S.; Lee, M.; Ben-Yakar, A. *J. Phys. D: Appl. Phys.* **2008**, *41* (18), 185501.
(48) Link, S.; Burda, C.; Nikoobakht, B.; El-Sayed, M. A. *J. Phys. Chem. B* **2000**, *104* (26), 6152−6163.
(49) Ben-yakar, A.; Eversole, D.; Ekici, O. In *Non-Magnetic Metallic Nanomaterials for Life Sciences of the 10 volume series on Nanomaterials for Life Sciences*; Wiley-VCH Verlag GmbH & Co. KGaA: Weinheim, 2008, pp 493−539.
(50) Lachaine, R.; Boulais, E.; Bourbeau, E.; Meunier, M. *Appl. Phys. A: Mater. Sci. Process.* **2013**, *112* (1), 119−122.
(51) Boutopoulos, C.; Hatef, A.; Fortin-Deschênes, M.; Meunier, M. *Nanoscale* **2015**, *7* (27), 11758−11765.
(52) Boulais, É.; Lachaine, R.; Meunier, M. *J. Phys. Chem. C* **2013**, *117* (18), 9386−9396.
(53) Patskovsky, S.; Bergeron, E.; Meunier, M. *J. Biophotonics* **2015**, *8* (1−2), 162−167.
(54) Boutopoulos, C.; Bergeron, E.; Meunier, M. *J. Biophotonics* **2016**, *9* (1−2), 26−31.
(55) Schaeublin, N. M.; Braydich-Stolle, L. K.; Schrand, A. M.; Miller, J. M.; Hutchison, J.; Schlager, J. J.; Hussain, S. M. *Nanoscale* **2011**, *3* (2), 410−420.
(56) McInnes, C. *Curr. Opin. Chem. Biol.* **2007**, *11* (5), 494−502.
(57) Lounnas, V.; Ritschel, T.; Kelder, J.; McGuire, R.; Bywater, R. P.; Foloppe, N. *Comput. Struct. Biotechnol. J.* **2013**, *5* (6), 1−14.
(58) Olivares-Amaya, R.; Amador-Bedolla, C.; Hachmann, J.; Atahan-Evrenk, S.; Sánchez-Carrera, R. S.; Vogt, L.; Aspuru-Guzik, A. *Energy Environ. Sci.* **2011**, *4* (12), 4849.

DOI: 10.1021/acs.nanolett.6b00562
Nano Lett. 2016, 16, 3187−3194